Broadband Nanoscale Surface-Enhanced Raman Spectroscopy by Multiresonant Nanolaminate Plasmonic Nanocavities on Vertical Nanopillars

*Meitong Nie, Yuming Zhao, Wonil Nam, Junyeob Song, Wengqi Zhu, Henri J. Lezec, Amit Agrawal, and Wei Zhou**

M. Nie, Y. Zhao, W. Nam, Prof. W. Zhou
Department of Electrical and Computer Engineering
Virginia Tech
Blacksburg, VA 24061, USA
E-mail: wzh@vt.edu

Dr. J. Song, Dr. W. Zhu, Dr. H. J. Lezec, Dr. A. Agrawal
Physical Measurement Laboratory
National Institute of Standards and Technology
Gaithersburg, MD 20899, USA

Keywords: multiresonant plasmonics, multi-band SERS, nanolaminate plasmonics, spatial mode overlap, surface-enhanced Raman spectroscopy

Surface-enhanced Raman spectroscopy (SERS) has become a sensitive detection technique for biochemical analysis. Despite significant research efforts, most SERS substrates consisting of single-resonant plasmonic nanostructures on the planar surface suffer from limitations of narrowband SERS operation and unoptimized nano-bio interface with living cells. Here, we report that nanolaminate plasmonic nanocavities on three-dimensional (3D) vertical nanopillar arrays can support a broadband SERS operation with large enhancement factors ($> 10^6$) under laser excitations at 532 nm, 633 nm, and 785 nm. The multi-band Raman mapping measurements show that nanolaminate plasmonic nanocavities on vertical nanopillar arrays exhibit broadband uniform SERS performance with diffraction-limited resolution at a single

nanopillar footprint. By selective exposure of embedded plasmonic hotspots in individual metal-insulator-metal (MIM) nanogaps, we demonstrate nanoscale broadband SERS operation at the single MIM nanocavity level with visible and near-infrared (vis-NIR) excitations. Numerical studies reveal that nanolaminate plasmonic nanocavities on vertical nanopillars can support multiple hybridized plasmonic modes to concentrate optical fields across a broadband wavelength range from 500 nm to 900 nm at the nanoscale.

1. Introduction

Surface-enhanced Raman spectroscopy (SERS), combining the molecular fingerprinting specificity of vibrational spectroscopy with the hotspot sensitivity of plasmonic nanostructures, can serve as an ultrasensitive bioanalytical detection technique.[1] Conventional SERS substrates with single-resonant plasmonic nanostructures can provide high SERS enhancement factors (EFs $>10^6$) within a restricted excitation wavelength range.[2] Recent studies show that multi-band SERS measurements under multiple excitation wavelengths can empower multiplexed detection of multiple analytes for complex samples.[3] In this regard, it is highly desirable to develop broadband multiresonant plasmonic systems for multi-band SERS measurements under different laser excitations. Notably, by spectrally matching the wavelengths among the excitation laser, plasmon resonance, and analyte absorption peak, multiresonant plasmonic systems can allow the surface-enhanced resonant Raman spectroscopy (SERRS) with an extra 10 to 100 fold signal intensity increment than the nonresonant SERS.[3c, 4] Since analyte molecules possess characteristic electronic transition features in addition to their vibrational fingerprints, multi-band SERS measurements under multiple excitation wavelengths can provide combined electronic and vibrational spectral information to enable a higher dimensional biochemical analysis of complex samples with multiple analytes.[3a]

For SERS bioanalysis of living cells, it is imperative to achieve intimate interfacing of plasmonic hotspots with the cell membrane[5] to enable direct probing of membrane organelles[6] and minimally invasive intracellular nanosurgery.[7] Recent studies have shown that protruding nanopillar structures with large local curvatures can activate mammalian cell engulfment machinery to promote an intimate nanodevice-cell coupling.[8] Notably, vertical nanopillar nanoelectrodes can trigger cellular engulfment activities for neurons and cardiomyocytes to create a tight resistive sealing and achieve intracellular-like electrical signal recording.[9] Unfortunately, existing nanopillar-shaped plasmonic nanostructures, such as hollow metal nano-straws,[10] 3D nanowire-like structures,[11] vertically aligned carbon nanotubes,[12] and mushroom-shaped vertical structures,[13] still face the design-fabrication constraints for seamless integration of multiresonant plasmonic nanostructures with predefined nanopillar array in multi-band SERS sensing of living cells.

The current design strategy for multi-band SERS substrates is to densely pack multiple plasmonic building blocks with different resonant wavelengths, such as different-sized Ag nanoparticles on glass-Ag-glass multilayers,[14] different-shaped plasmonic metal nanoparticles on Ag gratings,[15] random Ag nanoparticles on Au nano-bow arrays,[16] and width-graded arrays of plasmonic nanogratings.[17] Despite the simplicity in fabrication, these multi-band SERS substrates suffer from several limitations to integrate with nanopillars, including (1) large footprint due to the in-plane arrangement of multiple plasmonic building blocks; (2) limited spatial overlaps of different plasmonic modes; (3) difficult geometric control of plasmonic resonance properties, and (4) poor spatial uniformity of SERS hotspots.

In this study, we first characterized the multi-band SERS performance of the nanolaminate plasmonic nanocavities on high-aspect-ratio nanopillar arrays under laser excitations at 532 nm, 633 nm, and 785 nm. Next, we partially etched the dielectric layers and exposed the embedded

hotspots in the nanocavities to analytes, leading to several times improvement in SERS enhancement factors (EFs) in multi-band SERS measurements. Then, we selectively etched one individual dielectric layer and observed that the spatial mode distribution among three MIM nanogaps strongly depends on excitation laser wavelength. Last, numerical simulation studies revealed that the observed nanoscale broadband SERS performance is due to multiple spectrally separated and spatially overlapped hybrid plasmonic modes in nanolaminate plasmonic nanocavities over a broad vis-NIR spectral range. Our results show that multiresonant nanolaminate plasmonic nanocavities on high-aspect-ratio nanopillar arrays allow high-performance multi-band SERS operation between 500 nm and 900 nm at the single nanocavity level (Fig. 1A). Compared with conventional planar or low-aspect-ratio plasmonic nanostructures,[18] multiresonant nanolaminate plasmonic nanocavities on high-aspect-ratio vertical nanopillars can provide unique opportunities. First, the out-of-plane geometric engineering of vertically stacked nanolaminate plasmonic nanocavities can allow for precise and dense stacking of broadband multiresonant and spatially overlapped SERS hotspots within a nanoscale footprint. Second, integrating multiresonant plasmonic nanodevices with high-aspect-ratio nanopillars can activate engulfment machinery at the bio-nano interface for living mammalian cells, improving the SERS bioanalytical performance.[5] Third, nanolaminate plasmonic nanocavities can be integrated with predefined nanopillar electrode arrays for combined electrical recording and SERS monitoring of living cells. Fourth, multiresonant plasmonic nanodevices with spatial overlaps can potentially enable wavelength-multiplexed multifunctional nanophotonics and multiphoton nonlinear plasmonics.[19]

2. Result and Discussion

Fig. 1B illustrates the top-down scalable fabrication process to create Ag/SiO_2/Ag nanolaminate plasmonic nanostructures on predefined vertical nanopillar arrays. Briefly, the predefined

polyurethane (PU) polymer nanopillar array with a diameter of ≈ 100 nm, a height of ≈ 400 nm, and a pitch of ≈ 400 nm was replicated from nanowell-array structured polydimethylsiloxane (PDMS) stamp by nanoimprinting lithography. Next, we employed physical vapor evaporation to deposit alternating thin films of Ag (≈ 30 nm thickness) and SiO_2 (≈ 6 nm, ≈ 8 nm, and ≈ 12 nm thicknesses from bottom to top, respectively) on the PU nanopillar array, followed by an outer oxidation protection SiO_2 layer (≈ 30 nm thickness). The dark appearance in the top-view optical image and the vivid diffraction pattern in the tilted-view optical image (Fig. 1C) manifest a broadband absorption in the visible range and uniform distribution of nanostructures on the substrate. The top-view and cross-sectional scanning electron microscopy (SEM) images in Figures 1D, 1E and S1 illustrate the periodic nanopillar structures and multilayered MIM geometries of the fabricated samples. The design and fabrication of plasmonic MIM nanocavities on high-aspect-ratio nanopillars are desirable to achieve intimate interfacing with the cell membrane in biosensing applications. Notably, by wet etching of SiO_2 layers with buffered oxide etchant (BOE), the edges of SiO_2 layers were partially etched away, and the embedded hotspots in MIM nanogaps were exposed to analytes, as shown in Fig. 1F. We used an etching time of 15 s to prevent over-etching of SiO_2 layers and maintain the mechanical stability of MIM nanogaps on nanopillars (Fig. S2).

To examine multi-band SERS performance, we measured the SERS spectra from Ag/SiO_2/Ag samples with surface-modified benzenethiol (BZT) monolayer, a nonresonant Raman probe molecule.[20] Figures 2A, 2B, and 2C show the averaged BZT SERS spectra from 1200 pixels over three 20 μm × 20 μm regions on the nonetched Ag/SiO_2/Ag sample under 532 nm, 633 nm, and 785 nm excitations, respectively. We determined SERS EFs for BZT vibrational modes at 422 cm^{-1}, 700 cm^{-1}, 1001 cm^{-1}, 1026 cm^{-1}, 1077 cm^{-1}, and 1576 cm^{-1} by the formula: SERS EF $= (I_{SERS}/N_{SERS})/(I_{Raman}/N_{Raman})$, where I_{SERS}, I_{Raman}, N_{SERS}, and N_{Raman} are

the BZT SERS intensity, neat BZT Raman intensity, and the number of BZT molecules contributing to BZT SERS and neat BZT Raman intensities, respectively. According to the electromagnetic enhancement mechanism, the SERS EF for a molecule inside a hotspot can be expressed as:

$$\text{SERS EF}(\omega_0 - \Delta\omega_m) = g(\omega_0)^2 \cdot g(\omega_0 - \Delta\omega_m)^2 \cdot \eta_m \quad (1)$$

where ω_0 is excitation laser frequency, $\Delta\omega_m$ is Stokes-shifted frequency for a specific vibrational mode, g is the local electric field enhancement factor, and η_m is the coefficient related to the orientation of transition dipole moment for a specific vibrational mode regarding the direction of the local electric field. We can find several vital points from experimentally determined SERS EFs for different BZT Raman modes. First, the values of SERS EFs vary between different BZT Raman peaks under the same laser excitation wavelength. For example, under 532 nm laser excitation, SERS EFs for 422 cm^{-1}, 1077 cm^{-1}, and 1576 cm^{-1} (marked by an asterisk in Fig. 2A) are higher than those for 700 cm^{-1}, 1001 cm^{-1}, and 1026 cm^{-1} (marked by a cross in Fig. 2A). This observation reveals that different vibrational modes undergo different SERS EFs due to the difference in their orientation related coefficients η_m. Considering the immobilized orientation of densely packed BZT monolayer on Ag surface,[21] not all vibrational modes can be equally enhanced, and the vibrational modes perpendicular to the Ag surface are more enhanced than the vibrational modes in parallel with the Ag surface. By averaging the SERS EFs among different peaks, we can reduce the molecular orientation effect to approximate the plasmonic local field enhancement factor $g(\omega_0)^2 \cdot g(\omega_0 - \Delta\omega_m)^2$. Accordingly, we obtain an average SERS EFs of $(2.3 \pm 0.2) \times 10^5$, $(6.6 \pm 1.0) \times 10^5$, and $(5.3 \pm 0.9) \times 10^5$ under 532 nm, 633 nm, and 785 nm excitation, respectively. The uncertainties are one standard deviation obtained from 1200 individual pixels. Second, the SERS EFs are different for the same vibrational mode under different excitation laser wavelengths, revealing

the spectrally dispersive nature of the local field enhancement factor $g(\omega_0)^2 \cdot g(\omega_0 - \Delta\omega_m)^2$ associated with the multiresonant properties of plasmonic nanostructures. Figures 2D, 2E, and 2F show the BZT SERS spectra and SERS EFs for different BZT Raman peaks from BOE etched Ag/SiO_2/Ag samples under different laser excitation wavelengths. The average SERS EFs of etched Ag/SiO_2/Ag samples are (1.3 ± 0.2) × 10^6, (2.0 ± 0.3) × 10^6, and (2.8 ± 0.3) × 10^6 under 532 nm, 633 nm, and 785 nm excitations, which are approximately (5.5 ± 1.1), (3.0 ± 0.6), and (5.3 ± 1.1) times as high as SERS EFs for nonetched samples under associated laser excitations respectively. The uncertainties are one standard deviation based on the propagation of uncertainties from 1200 individual pixels. This observation reveals that more hotspots in the nanogaps become accessible to analytes contributing to an improved SERS EF. These newly exposed resonant nanogap SERS hotspots on vertical nanopillars can be engulfed by cell membrane to enable effective multi-band SERS molecular profiling of membrane protein biomarkers in biomedical applications.

To examine the spatial uniformity of multi-band SERS responses for the Ag/SiO_2/Ag nanolaminate sample, we conducted two-dimensional (2D) confocal Raman mapping over the same sample area under excitations at 532 nm, 633 nm, and 785 nm (Fig. 3). As shown in Fig. 3A, we created an L-shape imaging marker by photothermal burning under a high-power focused laser beam to allow accurate position registration in 2D Raman maps (yellow dashed square, 35 μm × 35 μm) measured under the three excitation wavelengths. Figures 3B, 3C, and 3D illustrate the 2D maps of measured SERS EFs for the 1077 cm^{-1} BZT peak from the same sample area under 532 nm, 633 nm, and 785 nm excitations, manifesting a uniform distribution for broadband high-performance SERS responses. Interestingly, the L-shaped marker region exhibits higher SERS EFs under 633 nm and 785 nm excitations and lower SERS EFs under 532 nm excitation than the rest because the geometric disruption from laser photothermal

damage can change the multiresonant plasmonic properties. Fig. 3E shows the SERS EF scatter plot and the histograms for the BZT 1077 cm^{-1} Raman peak from 400 pixels within the same 20 μm × 20 μm area (black dashed square in Figures 3B, 3C, and 3D) under 532 nm, 633 nm, and 785 nm excitations. The simultaneously high and uniform SERS EFs under three laser excitation wavelengths suggest that nanolaminate plasmonic nanostructures can support multiple resonant modes with spatial overlap within the optical diffraction limit (≈ 655 nm) in measurements.

To further investigate the multi-band SERS response within individual MIM nanogap, we created Ag/SiO_2/MgF_2/Ag nanolaminate plasmonic nanostructures consisting of MgF_2 and SiO_2 as two different insulator materials in MIM nanocavities (Fig. 4A). Specifically, the bottom two insulator layers of MgF_2 are non-etchable by HF during the BOE wet etching process. Also, MgF_2 has a refractive index ranging from 1.37 to 1.39 in the vis-NIR range, slightly smaller than the refractive index of SiO_2 (1.45 to 1.48), and thus the optical properties of the nanolaminate plasmonic systems do not change a lot. As confirmed in the SEM images (Fig. 4B), a 15 s BOE etching process can partially expose the nanogap embedded hotspots associated with the top SiO_2 layer but not those associated with the middle and bottom MgF_2 layers. To evaluate the optical near field enhancement associated with hotspots in the top SiO_2 nanogap, we measured SERS signals from BZT self-assembled Ag/SiO_2/MgF_2/Ag samples under the same experimental conditions as in Fig. 2 for Ag/SiO_2/Ag samples. Before BOE etching, as shown in Fig. 4C, BZT SERS signals from the Ag/SiO_2/Ag and Ag/SiO_2/MgF_2/Ag samples have similar intensities under 532 nm, 633 nm, and 785 nm excitations. According to eq. 1, Ag/SiO_2/Ag and Ag/SiO_2/MgF_2/Ag samples before BOE etching share the same molecule orientation coefficient η_m, and their SERS EFs primarily depend on the optical near-field enhancement term of $g(\omega_0)^2 \cdot g(\omega_0 - \Delta\omega)^2$. Therefore, for Ag/$SiO_2$/Ag and

Ag/SiO_2/MgF_2/Ag samples before BOE etching, their similar SERS intensities under different excitation wavelengths reveal their similar multiresonant plasmonic near-field enhancement responses in $g(\omega_0)^2 \cdot g(\omega_0 - \Delta\omega)^2$ before geometric changes by etching SiO_2 layers in nanogap. As shown in Figures 4D, 4E, and 4F, after a 15 s BOE etching, the averaged SERS EFs of Ag/SiO_2/MgF_2/Ag samples increased to approximately (3.3 ± 0.5), (2.6 ± 0.4), and (3.5 ± 0.5) times compared to the nonetched sample under 532 nm, 633 nm, and 785 nm excitations, respectively. The uncertainties are one standard deviation based on the propagation of uncertainties from 1200 individual pixels. The partial exposure of the top nanogap embedded hotspots causes such multi-band SERS EF improvement under different excitation wavelengths over the vis-NIR spectral range.

While the SERS EF increment originates from the top nanogap hotspots for the Ag/SiO_2/MgF_2/Ag samples, the SERS EF increment comes from hotspots in all three nanogaps for the Ag/SiO_2/Ag samples. As shown in Fig. 4G, the SERS EF increment of the Ag/SiO_2/Ag samples (outlined by the black rectangle) can be decomposed into the contributions from the top nanogap hotspots (orange box) and the rest of the middle and the bottom nanogap hotspots (light orange box). Suppose we approximate the SERS EF increment associated with the exposed top nanogap hotspots (orange box) in the Ag/SiO_2/Ag samples with the SERS EF increment contributed by top SiO_2 nanogap hotspots in the Ag/SiO_2/MgF_2/Ag samples, we can retrieve the relative ratio of SERS EF contributions among different nanogaps in the Ag/SiO_2/Ag samples. As shown in Fig. 4G, under 532 nm and 785 nm excitations, the SERS EF contributions from the top nanogap hotspots are similar to the combination of middle and bottom nanogap hotspots. Nevertheless, under 633 nm excitation, the SERS EF contributions are dominantly from the top nanogap hotspots, indicating the significant dependence of the spatial mode distribution among the three MIM nanogaps on excitation laser wavelength.

To investigate the multiresonant properties of nanolaminate plasmonic nanocavities on vertical nanopillars, we have measured far-field reflectance and transmittance spectra of Ag/SiO_2/Ag (Figures 5A and S3A) and Ag/SiO_2/MgF_2/Ag (Figures 5B and S3B) samples. The reflectance spectra (Fig. 5A) of the Ag/SiO_2/Ag sample exhibit multiple dips at 435 nm, 534 nm, 623 nm, 685 nm, 706 nm, and 919 nm. The Ag/SiO_2/MgF_2/Ag sample (Fig. 5B) shows a similar reflectance spectrum with multiple dips at 435 nm, 565 nm, 662 nm, 710 nm, and 811 nm. This observation reveals that the minor refractive index change from SiO_2 (1.45 to 1.48) to MgF_2 (1.37 to 1.39) in nanogap layers has a limited effect on the multiresonant optical properties of nanolaminate plasmonic nanocavities on vertical nanopillars. Moreover, we have calculated the far-field and near-field optical properties using the finite-difference time-domain (FDTD) method. Our calculations illustrate that Ag/SiO_2/Ag and Ag/SiO_2/MgF_2/Ag samples exhibit similar reflectance spectra (red lines in Figures 5A and 5B) with multiple resonant dips, agreeing with the measurements. The measurements show resonant features with broader linewidths than the calculations. It should be noted that the reflectance spectra are measured over a spot size of 12.50 mm × 7.11 mm containing 5.55×10^8 plasmonic nanopillar units. As seen in the SEM images (Figures 1 and S1), the geometric variations between individual nanopillars and plasmonic nanocavities can cause the inhomogeneous broadening effect, which is the dominant factor causing the broader linewidth in the measurements. Moreover, the increased metal losses associated with the interface roughness between metal and dielectric layers would cause the homogeneous broadening effect.

To understand the microscopic resonant behaviors, we calculated the optical response of the two subsystems, nanolaminate nanoparticle arrays (Fig. 5C) and nanolaminate nanohole arrays (Fig. 5D), in comparison with the coupled system (Fig. 5E). Fig. 5C shows that nanolaminate nanoparticle arrays support three dominant absorption peaks attributed to diffraction lattice

mode at $\lambda_{NPA-1} \approx 447$ nm, the electric dipole (ED) mode at $\lambda_{NPA-2} \approx 543$ nm, and the magnetic dipole (MD) mode at $\lambda_{NPA-3} \approx 1047$ nm (Fig. S4). On the other hand, as shown in Fig. 5D, nanolaminate nanohole arrays exhibit four absorption peaks associated with three bottom metal-polymer interface Bloch surface plasmon polariton (SPP) modes: (± 2, ± 2) at $\lambda_{NHA-1} \approx 425$ nm, (± 1, ± 1) at $\lambda_{NHA-2} \approx 515$ nm, and (± 1, 0) at $\lambda_{NHA-3} \approx 704$ nm as well as one hybridized nanogap Bloch SPP mode (± 1, ± 1) at $\lambda_{NHA-4} \approx 971$ nm (Fig. S5). For the coupled system of nanolaminate nanocavities on nanopillar arrays, as shown in Fig. 5E, we can observe six absorption peaks at resonant wavelengths correlated with the modes in their subsystems of nanolaminate nanoparticle arrays and nanolaminate nanohole arrays, manifesting that their multiresonant responses originate from the plasmonic hybridization between elementary modes in the two subsystems in far-field coupling regime.[22] FDTD-calculated near-field mode profiles in Fig. 5F confirm that the modes in nanolaminate nanocavities on nanopillar arrays show mode distribution profiles with spatial correlation with elementary modes in their two uncoupled subsystems (Fig. S6). Specifically, the hybrid mode at λ_1 exhibits a relatively weak field enhancement due to the weak local field confinement of the lattice plasmon mode (λ_{NPA-1}) and weak coupling efficiency with free-space light of the high order Bloch SPP mode (λ_{NHA-1}). The hybrid modes at λ_2, λ_3, and λ_4 show concentrated electric field inside the insulator layers of the nanolaminate nanoparticles since the ED LSP mode (λ_{NPA-2}) is strongly excited by the spectrally well-aligned Bloch SPP mode (λ_{NHA-2}) through the far-field coupling. In contrast, the hybrid mode at λ_5 is weakly excited at the nanolaminate nanoparticle part but concentrated at the bottom of the nanolaminate nanohole arrays because the off-resonant ED LSP mode (λ_{NPA-2}) only weakly couples with the on-resonant Bloch SPP mode (λ_{NHA-3}). The hybrid mode at λ_6 is mainly located in the insulator layers in nanolaminate nanohole arrays since the MD LSP mode (λ_{NPA-3}) is weakly excited through far-field coupling due to its low quantum yield compared to the hybridized Bloch SPP mode (λ_{NHA-4}). Across the spectral range in multi-

band SERS measurements between 500 nm and 900 nm (shaded with blue in Fig. 5E), the multiresonant features are primarily associated with the hybrid modes λ_2 to λ_5, where the molecule-accessible nanogap hotspots are primarily in nanolaminate nanocavities on vertical nanopillars. Notably, the nanolaminate plasmonic nanoparticle array with increased pitch sizes can still have the multiresonant responses with substantial local field enhancement due to the hybridization between localized plasmonic modes in the stacked MIM building blocks with different insulator thicknesses.[23] This feature also benefits SERS analysis of living cells because a low lattice density of the vertical nanopillar arrays will promote stable cell adhesion and trigger cells into a less motile state,[24] facilitating direct SERS molecular profiling of membrane protein biomarkers.

To understand the difference of spatial mode distribution between three insulator nanogaps in nanolaminate nanocavities on vertical nanopillars, we conducted FDTD simulations with three center-to-edge line monitors placed within three individual nanogaps (Fig. 6A). As depicted in Figures 6B, 6C, and 6D, the mode profiles ($|E^2|$) show a spectral dispersion in each nanogap. Interestingly, the spectral dispersion behaves differently in each nanogap. Specifically, from 600 nm to 700 nm the $|E^2|$ distributes unimodally in the top nanogap but bimodally in the middle and bottom nanogaps, as the dashed lines noted, revealing different mode natures in these three nanocavities. In the bottom nanogap, there is a phase flip of the electric field across 600 nm to 700 nm (Fig. S7), resulting in a transition from a magnetic quadrupole (MQ) LSP mode to MD LSP mode and consequently the bimodal characteristics of the $|E^2|$ profile in the middle and bottom nanogaps. In contrast, the fields inside the top nanogap maintain the MD mode nature with a unimodal $|E^2|$ distribution across 600 nm to 700 nm. We further quantified the SERS EF contributed by each nanogap as

$$\mathrm{EF}_i(\lambda_0,\lambda)=\sum_j|\boldsymbol{r_j}|\left|\frac{E(\boldsymbol{r_j},\lambda_0)}{E_0(\boldsymbol{r_j},\lambda_0)}\right|^2\left|\frac{E(\boldsymbol{r_j},\lambda)}{E_0(\boldsymbol{r_j},\lambda)}\right|^2$$

where *i* is the notation of the gap, λ_0 is the excitation wavelength, λ is the emission wavelength, $\boldsymbol{r_j}$ is the position vector in the specific insulator gap with an estimated etching depth (10 nm) from the gap edge, and the $|\boldsymbol{r_j}|$ is the weight related to the molecule adsorption surface area. The enhancement factor ratio between the top nanogap and combination of the middle and bottom nanogaps can be approximated as $R=\mathrm{EF}_{\mathrm{top}}(\lambda_0,\lambda)/[\mathrm{EF}_{\mathrm{middle}}(\lambda_0,\lambda)+\mathrm{EF}_{\mathrm{bottom}}(\lambda_0,\lambda)]$ as plotted in Fig. 6E. The ratio, *R*, is spectrally dispersive and higher at 633 nm than at 532 nm and 785 nm, agreeing with our experimental observations (Fig. 4G).

3. Conclusion

In summary, we demonstrate that MIM nanolaminate plasmonic nanocavities on high-aspect-ratio nanopillar arrays can achieve high SERS EFs (> 10^6) over a broad spectral range (500 nm to 900 nm) with multiresonant optical concentration at the single nanocavity level. Such nanolaminate plasmonic nanostructures can provide a multi-band uniform and reproducible SERS signal with a small footprint by accurate nanoscale control of vertically oriented plasmonic nanogap geometries, desirable for multi-band SERS applications. Our measurements and calculations reveal that the individual nanolaminate nanocavities can support multiple resonance modes over a broad wavelength range with substantial near-field enhancement. The multiresonant nanolaminate plasmonic nanostructures can allow multi-band SERS/SERRS operation under different laser excitations from 500 nm to 900 nm, potentially enabling high-dimensional biochemical analyses by providing combined electronic and vibrational molecular information. Furthermore, nanolaminate plasmonic nanocavities can easily integrate with vertical nanopillar electrode arrays for combined electrical recording and SERS monitoring of

living cells. Beyond multi-band SERS applications, multiresonant nanolaminate substrates can serve as wavelength-multiplexed multifunctional plasmonic nanotransducers at the subcellular level with different optical modalities. Our studies suggest that nanolaminate plasmonic nanostructures on high-aspect-ratio nanopillar arrays can allow the simultaneous nanolocalized enhancement of both excitation and emission transitions in multiphoton nonlinear processes across a broad wavelength range, opening exciting avenues toward cell-interfaced nonlinear nano-optics sensing/spectroscopy/imaging applications.

4. Experimental Section

Sample fabrication: A composite polydimethylsiloxane (PDMS) stamp was replicated from a Si master with vertical nanopillar arrays (100 nm in diameter, 400 nm in height, and 400 nm in period) by soft lithography.[25] Then, a UV-curable polyurethane (PU) nanopillar array was replicated on a polyester film from the PDMS stamp by UV curing for 5 min, followed by heat-curing at 80 ℃ overnight. Next, alternative Ag and SiO_2 (or MgF_2) thin films were deposited on the PU nanopillar arrays by physical vapor evaporation with designed thickness. Also, 1 nm thick Cr between polymer nanopillar array and the first Ag layer, and 0.7 nm thick Ti between metal and insulator layers were deposited to improve the adhesion.

SERS characterization: We used a confocal Raman microscope equipped with 532 nm, 633 nm, and 785 nm lasers for multi-band SERS measurement. To form a BZT monolayer, we incubated the SERS substrates in 1 mol m^{-3} BZT ethanolic solution for 24 h, followed by ethanol rinsing. Back-scattered Raman signals were collected via a 20× objective (NA = 0.4) with 0.1 s integration time. The laser power intensities were 0.1 mW, 0.1 mW, and 2 mW for 532 nm, 633 nm, and 785 nm measurements, respectively.

SERS EF calculation: SERS EFs were calculated by $\text{SERS EF} = (I_{SERS}/N_{SERS})/(I_{Raman}/N_{Raman})$, where I_{SERS}, I_{Raman}, N_{SERS}, N_{Raman} are the BZT SERS intensity, neat BZT Raman intensity, and the number of BZT molecules contributing to BZT SERS and neat BZT Raman intensities, respectively.[26] N_{SERS} was calculated by $N_{SERS} = SA \times \rho_{SERS}$, where SA is the metal surface area contributing to the SERS enhancement, and ρ_{SERS} is the molecule packing density of BZT monolayer on the Ag NP surface (3.3×10^{14} cm^{-2}).[27] N_{Raman} was calculated with $N_{Raman} = A \times d_{eff} \times \rho_{BZT}$, where A is the focused laser beam area, d_{eff} is the effective depth of the laser beam spot under 20× objective, and ρ_{BZT} is the neat BZT molecule density (5.9×10^{21} cm^{-3}). For I_{SERS} and I_{Raman}, six major Raman peaks at 422 cm^{-1}, 700 cm^{-1}, 1001 cm^{-1}, 1026 cm^{-1}, 1077

cm^{-1}, and 1576 cm^{-1} were selected to calculate the SERS EF, which correspond to the carbon-sulfur (C-S) stretching and carbon-carbon-carbon (C-C-C) ring in-plane deformation vibration, C-C-C ring in-plane bending with C-S stretching mode, the C-C-C ring in-plane bending mode, the carbon-hydrogen (C-H) in-plane bending mode, the C-C-C ring in-plane breathing mode with C-S stretching mode, and the C-S stretching mode for BZT molecules.[28]

Far-field reflectance and transmittance measurement: The reflectance and transmittance spectra of samples were measured by a UV−vis−near-infrared (NIR) spectrophotometer. In reflectance measurement, the specular and diffuse reflections are collected by an integrating sphere with an incidence angle of 3.33°.

Numerical simulations: A cone-shape nanoparticle and a beveled nanohole were adopted to mimic the shadowing effect in the deposition. A uniform mesh size of 1 nm (in x, y, and z directions) was used. The Bloch boundary condition was used in x- and y-directions with a periodicity of 400 nm, and the perfectly matched layer boundary condition was used in the z-direction. A normal-incident plane wave source was used to mimic the incidence angle in far-field reflectance measurement. The dielectric function of silver was obtained from the Palik handbook of optical constants for solids.[29]

Acknowledgements

M. Nie and Y. Zhao contributed equally to this work. This work was partially supported by US AFOSR Young Investigator Award FA9550-18-1-0328, US NSF grant DMR2139317, US NIST grant 70NANB18H201, and US NIST grant 70NANB19H163.

References

[1] a) J. Langer, D. Jimenez de Aberasturi, J. Aizpurua, R. A. Alvarez-Puebla, B. Auguié, J. J. Baumberg, G. C. Bazan, S. E. Bell, A. Boisen, A. G. J. A. n. Brolo, *ACS Nano* **2019**, *14*, 28; b) S. Schlucker, *Angew. Chem. Int. Ed.* **2014**, *53*, 4756; c) C. Zong, M. X. Xu, L. J. Xu, T. Wei, X. Ma, X. S. Zheng, R. Hu, B. Ren, *Chem. Rev.* **2018**, *118*, 4946.

[2] a) J. F. Li, Y. F. Huang, Y. Ding, Z. L. Yang, S. B. Li, X. S. Zhou, F. R. Fan, W. Zhang, Z. Y. Zhou, D. Y. Wu, B. Ren, Z. L. Wang, Z. Q. Tian, *Nature* **2010**, *464*, 392; b) C. Matricardi, C. Hanske, J. L. Garcia-Pomar, J. Langer, A. Mihi, L. M. Liz-Marzán, *ACS Nano* **2018**, *12*, 8531; c) V. K. Rao, T. P. Radhakrishnan, *ACS Appl. Mater. Interfaces* **2015**, *7*, 12767.

[3] a) B. R. Lutz, C. E. Dentinger, L. N. Nguyen, L. Sun, J. Zhang, A. N. Allen, S. Chan, B. S. Knudsen, *ACS Nano* **2008**, *2*, 2306; b) J. A. Dougan, K. Faulds, *Analyst* **2012**, *137*, 545; c) W. E. Smith, *Chem. Soc. Rev.* **2008**, *37*, 955.

[4] a) G. Mcnay, D. Eustace, W. E. Smith, K. Faulds, D. Graham, *Appl. Spectrosc.* **2011**, *65*, 825; b) H. Cho, B. R. Baker, S. Wachsmann-Hogiu, C. V. Pagba, T. A. Laurence, S. M. Lane, L. P. Lee, J. B.-H. Tok, *Nano Lett.* **2008**, *8*, 4386.

[5] A. F. Mcguire, F. Santoro, B. Cui, *Annu. Rev. Anal. Chem.* **2018**, *11*, 101.

[6] a) M. D. Hodges, J. G. Kelly, A. J. Bentley, S. Fogarty, I. I. Patel, F. L. Martin, N. J. Fullwood, *ACS Nano* **2011**, *5*, 9535; b) H. Dong, D. Yao, Q. Zhou, L. Zhang, Y. Tian, *Chem. Commun.* **2019**, *55*, 1730; c) L. Xiao, K. A. Bailey, H. Wang, Z. D. Schultz, *Anal. Chem.* **2017**, *89*, 9091.

[7] a) E. A. Vitol, Z. Orynbayeva, M. J. Bouchard, J. Azizkhan-Clifford, G. Friedman, Y. Gogotsi, *ACS Nano* **2009**, *3*, 3529; b) J. J. Niu, M. G. Schrlau, G. Friedman, Y. Gogotsi, *Small* **2011**, *7*, 540; c) A. Huefner, W.-L. Kuan, R. A. Barker, S. Mahajan, *Nano Lett.* **2013**, *13*, 2463.

[8] a) W. Zhao, L. Hanson, H.-Y. Lou, M. Akamatsu, P. D. Chowdary, F. Santoro, J. R. Marks, A. Grassart, D. G. Drubin, Y. Cui, B. Cui, *Nat. Nanotechnol.* **2017**, *12*, 750; b) M. Dipalo, A. F. Mcguire, H.-Y. Lou, V. Caprettini, G. Melle, G. Bruno, C. Lubrano, L. Matino, X. Li, F. De Angelis, B. Cui, F. Santoro, *Nano Lett.* **2018**, *18*, 6100; c) A. Hai, D. Kamber, G. Malkinson, H. Erez, N. Mazurski, J. Shappir, M. E. Spira, *J. Neural Eng.* **2009**, *6*, 066009; d) F. Santoro, S. Dasgupta, J. Schnitker, T. Auth, E. Neumann, G. Panaitov, G. Gompper, A. Offenhäusser, *ACS Nano* **2014**, *8*, 6713.

[9] a) M. Dipalo, H. Amin, L. Lovato, F. Moia, V. Caprettini, G. C. Messina, F. Tantussi, L. Berdondini, F. De Angelis, *Nano Lett.* **2017**, *17*, 3932; b) A. Cerea, V. Caprettini, G. Bruno, L. Lovato, G. Melle, F. Tantussi, R. Capozza, F. Moia, M. Dipalo, F. De Angelis, *Lab Chip* **2018**, *18*, 3492.

[10] a) G. C. Messina, M. Dipalo, R. La Rocca, P. Zilio, V. Caprettini, R. Proietti Zaccaria, A. Toma, F. Tantussi, L. Berdondini, F. De Angelis, *Adv. Mater.* **2015**, *27*, 7145; b) J. J. Vandersarl, A. M. Xu, N. A. Melosh, *Nano Lett.* **2012**, *12*, 3881.

[11] H. C. Jeon, C.-J. Heo, S. Y. Lee, S.-M. Yang, *Adv. Funct. Mater.* **2012**, *22*, 4268.

[12] R. Liu, R. Chen, A. T. Elthakeb, S. H. Lee, S. Hinckley, M. L. Khraiche, J. Scott, D. Pre, Y. Hwang, A. Tanaka, Y. G. Ro, A. K. Matsushita, X. Dai, C. Soci, S. Biesmans, A. James, J. Nogan, K. L. Jungjohann, D. V. Pete, D. B. Webb, Y. Zou, A. G. Bang, S. A. Dayeh, *Nano Lett.* **2017**, *17*, 2757.

[13] a) N. Shmoel, N. Rabieh, S. M. Ojovan, H. Erez, E. Maydan, M. E. Spira, *Sci. Rep.* **2016**, *6*, 27110; b) S. M. Ojovan, N. Rabieh, N. Shmoel, H. Erez, E. Maydan, A. Cohen, M. E. Spira, *Sci. Rep.* **2015**, *5*, 14100.

[14] N. Zhang, K. Liu, Z. J. Liu, H. M. Song, X. Zeng, D. X. Ji, A. Cheney, S. H. Jiang, Q. Q. Gan, *Adv. Mater. Interfaces* **2015**, *2*, 1500142.

[15] Y. Kalachyova, D. Mares, V. Jerabek, K. Zaruba, P. Ulbrich, L. Lapcak, V. Svorcik, O. J. T. J. o. P. C. C. Lyutakov, *J. Phys. Chem. C* **2016**, *120*, 10569.

[16] P. Mao, C. Liu, G. Favraud, Q. Chen, M. Han, A. Fratalocchi, S. J. N. c. Zhang, *Nat. Commun.* **2018**, *9*, 1.

[17] N. Kazemi-Zanjani, M. Shayegannia, R. Prinja, A. O. Montazeri, A. Mohammadzadeh, K. Dixon, S. Zhu, P. R. Selvaganapathy, A. Zavodni, N. J. A. O. M. Matsuura, *Adv. Opt. Mater.* **2018**, *6*, 1701136.

[18] J. Song, W. Nam, W. J. A. M. T. Zhou, *Adv. Mater. Technol.* **2019**, *4*, 1800689.

[19] S. A. S. Tali, W. J. N. Zhou, *Nanophotonics* **2019**, *8*, 1199.

[20] a) N. G. Greeneltch, M. G. Blaber, G. C. Schatz, R. P. Van Duyne, *J. Phys. Chem. C* **2013**, *117*, 2554; b) X. Zhang, Y. Zheng, X. Liu, W. Lu, J. Dai, D. Y. Lei, D. R. Macfarlane, *Adv. Mater.* **2015**, *27*, 1090.

[21] a) J. Nara, S. I. Higai, Y. Morikawa, T. Ohno, *J. Chem. Phys.* **2004**, *120*, 6705; b) S. K. Saikin, R. Olivares-Amaya, D. Rappoport, M. Stopa, A. Aspuru-Guzik, *Phys. Chem. Chem. Phys.* **2009**, *11*, 9401.

[22] S. A. S. Tali, J. Song, W. Nam, W. Zhou, *Adv. Opt. Mater.* **2021**, *9*, 2001908.

[23] a) Y. Z. Qian, S. A. S. Tail, E. Mejia, W. Zhou, *Optik* **2021**, *230*, 166332; b) E. Mejia, Y. Qian, S. A. Safiabadi Tali, J. Song, W. Zhou, *Appl. Phys. Lett.* **2021**, *118*, 241108; c) J. Song, W. Zhou, *Nano Lett.* **2018**, *18*, 4409.

[24] H. Persson, Z. Li, J. O. Tegenfeldt, S. Oredsson, C. N. Prinz, *Sci. Rep.* **2015**, *5*, 18535.

[25] D. Qin, Y. N. Xia, G. M. Whitesides, *Nat. Protoc.* **2010**, *5*, 491.

[26] E. C. Le Ru, E. Blackie, M. Meyer, P. G. Etchegoin, *J. Phys. Chem. C* **2007**, *111*, 13794.

[27] J. Y. Gui, D. A. Stern, D. G. Frank, F. Lu, D. C. Zapien, A. T. Hubbard, *Langmuir* **1991**, *7*, 955.

[28] T. H. Joo, M. S. Kim, K. Kim, *J. Raman Spectrosc.* **1987**, *18*, 57.

[29] E. D. Palik, *Handbook of optical constants of solids*, Academic Press, Cambridge, MA, USA **1998**.

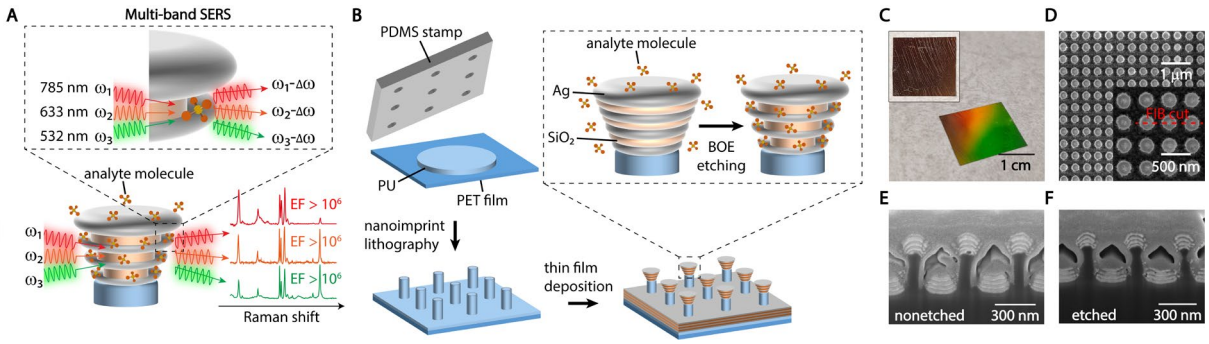

Figure 1. Multiresonant nanolaminate plasmonic nanocavities on vertical nanopillars. (A) Scheme of nanoscale multi-band SERS under multiple laser excitations. (B) The schematic fabrication process and illustration of Ag/SiO_2/Ag nanolaminate plasmonic nanocavities before and after BOE etching of SiO_2 layers. (C) Tilted-view and top-view (inset) optical camera images of the fabricated sample. (D) Top-view SEM images of nanolaminate plasmonic nanocavities on vertical nanopillars. (E-F) Cross-sectional view SEM images of nanolaminate plasmonic nanocavities on vertical nanopillars (E) before and (F) after 15 s BOE etching of SiO_2 layers. The cutting plane of Figure 1E is marked by the red dashed line labelled as focused ion-beam (FIB) cut in Figure 1D.

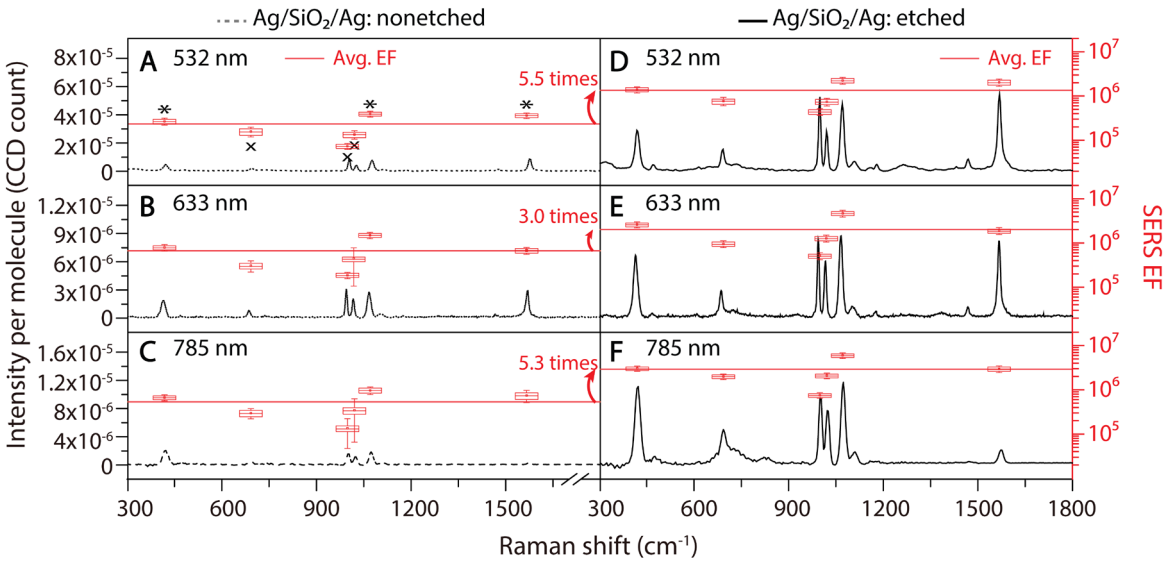

Figure 2. Multi-band SERS performance of $Ag/SiO_2/Ag$ nanolaminate plasmonic nanocavities on vertical nanopillars. (A-C) The average SERS spectra and corresponding SERS EFs of different BZT Raman peaks from the sample before BOE etching under (A) 532 nm, (B) 633 nm, and (C) 785 nm excitations. (D-E) The average SERS spectra and corresponding SERS EFs of different BZT Raman peaks from the sample after 15 s BOE etching under (D) 532 nm, (E) 633 nm, and (F) 785 nm excitations. The error bars show one standard deviation from 1200 pixels over three 20 μm × 20 μm regions. The bars in boxes from top to bottom represent 75th quartile, median, and 25th quartile values from 1200 pixels. The square represents the mean value.

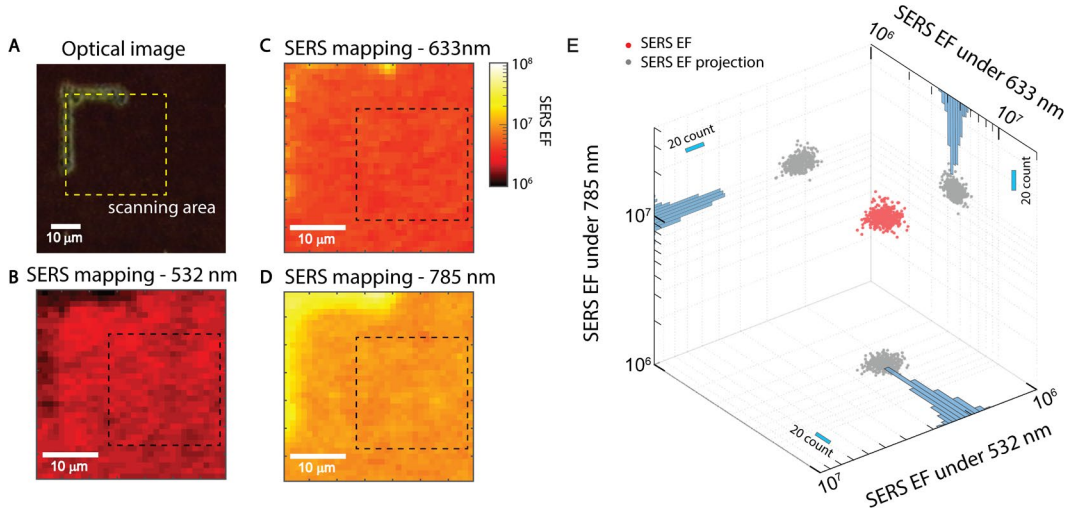

Figure 3. Uniform spatial distribution of multi-band SERS responses for Ag/SiO_2/Ag nanolaminate plasmonic nanocavities on vertical nanopillars. (A) Bright-field optical image and (B-D) scanning confocal SERS mapping images (at 1077 cm^{-1}) of the same region (marked as the yellow dashed square in Figure 3A) from the sample after 15 s BOE etching under (B) 532 nm, (C) 633 nm and (D) 785 nm excitations. (E) The three-dimension scatter plot and histograms of SERS EFs for the BZT Raman peak at 1077 cm^{-1} from individual laser beam locations within the black dashed region in Figures 3B-D under 532 nm, 633 nm, and 785 nm excitations.

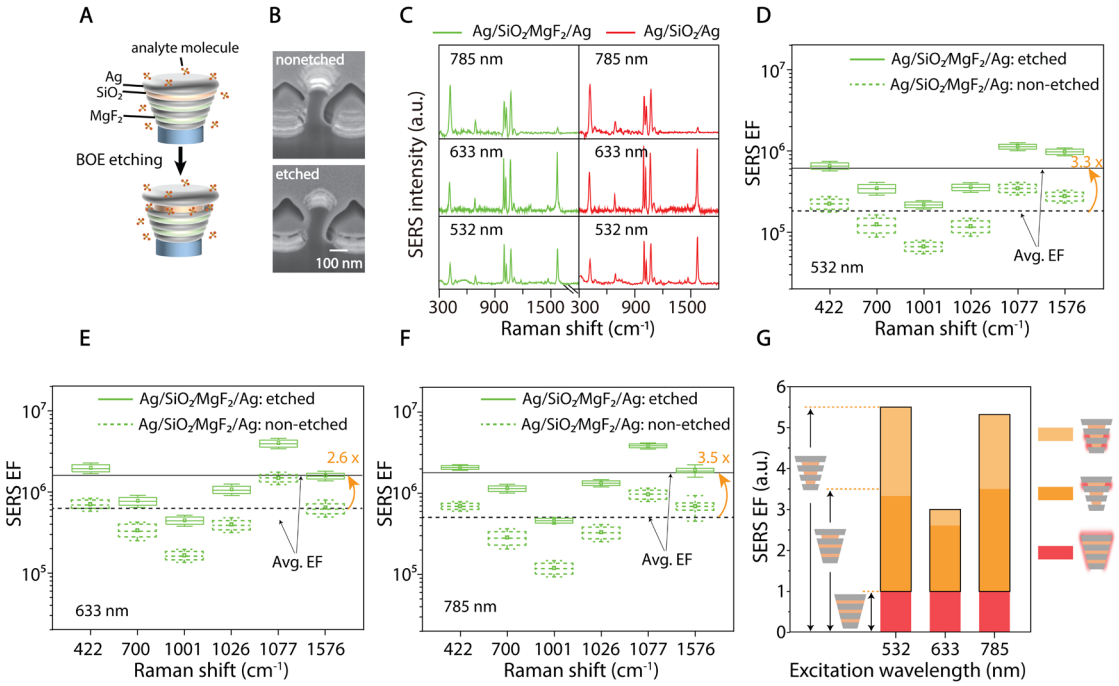

Figure 4. Multi-band SERS responses at a single MIM nanocavity level. (A) Schematic illustration of BOE etching of SiO_2 layer in $Ag/SiO_2/MgF_2/Ag$ nanolaminate plasmonic nanocavities on vertical nanopillars. (B) The cross-sectional view SEM images of $Ag/SiO_2/MgF_2/Ag$ sample before (nonetched) and after 15 s BOE etching of the SiO_2 layer. (C) The measured SERS spectra of BZT molecules from $Ag/SiO_2/MgF_2/Ag$ and $Ag/SiO_2/Ag$ samples under 532 nm, 633 nm, and 785 nm excitations with an etching time of 0 s. (D-F) The SERS EFs in box plots of different BZT Raman peaks from the $Ag/SiO_2/MgF_2/Ag$ sample before (nonetched) and after 15 s BOE etching of the SiO_2 layer under (D) 532 nm, (E) 633 nm, and (F) 785 nm excitations. The error bars represent one standard deviation from 1200 pixels over three 20 μm × 20 μm regions. The bars in boxes from top to bottom represent 75th quartile, median, and 25th quartile values from 1200 pixels. The square represents the mean value. (G) Normalized SERS EF increments after BOE etching of $Ag/SiO_2/Ag$ (outlined by the black rectangle) and $Ag/SiO_2/MgF_2/Ag$ (highlighted as orange) samples compared to nonetched samples (highlighted as red).

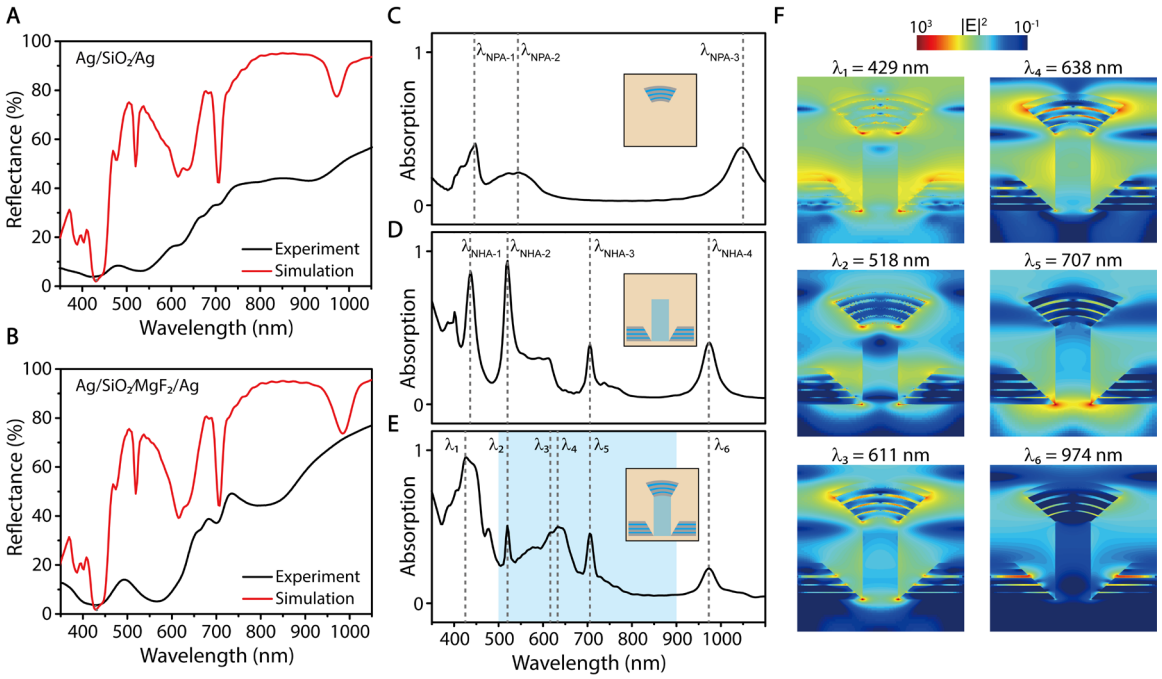

Figure 5. Far-field and near-field optical properties of the nanolaminate plasmonic nanocavities on vertical nanopillars. (A-B) Measured and FDTD-calculated reflectance spectra of (A) $Ag/SiO_2/Ag$ and (B) Ag/SiO2/MgF_2/Ag samples. (C-E) The FDTD-calculated absorption spectra for the two subsystems of (C) $Ag/SiO_2/Ag$ nanolaminate nanoparticle array and (D) $Ag/SiO_2/Ag$ nanolaminate nanohole array in comparison with (E) the coupled system of the $Ag/SiO_2/Ag$ sample. (F) FDTD-calculated x-z distribution maps of $|E|^2$ for plasmonic modes λ_1-λ_6 marked in (E).

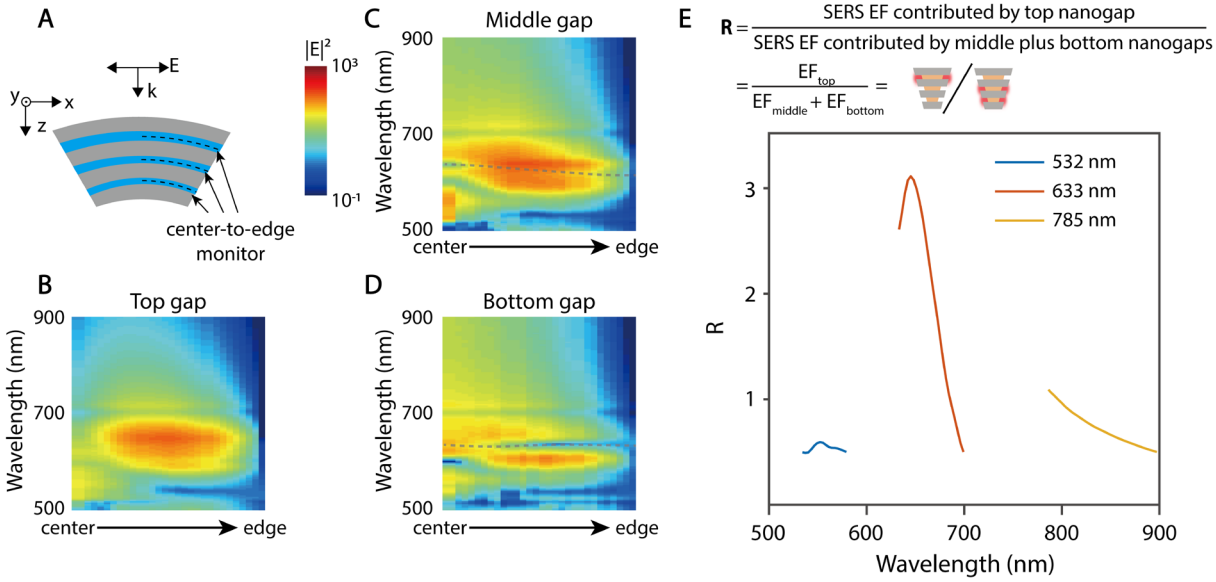

Figure 6. Near-field optical field enhancement inside MIM nanogaps. (A) Schematic of $Ag/SiO_2/Ag$ nanolaminate plasmonic nanocavities on vertical nanopillars with curved center-to-edge monitors under the polarized light illumination. (B-D) The FDTD-calculated spectral maps of near-field $|E|^2$ enhancement factor as a function of radial position from the center to the edge on the curved line monitor within (B) top, (C) middle, and (D) bottom nanogaps in the $Ag/SiO_2/Ag$ sample. (E) The ratio of calculated SERS enhancement factors between the top nanogap and the combination of middle and bottom nanogaps in the $Ag/SiO_2/Ag$ sample.

Supporting Information

Broadband Nanoscale Surface-Enhanced Raman Spectroscopy by Multiresonant Nanolaminate Plasmonic Nanocavities on Vertical Nanopillars

*Meitong Nie, Yuming Zhao, Wonil Nam, Junyeob Song, Wenqi Zhu, Henri J. Lezec, Amit Agrawal, and Wei Zhou**

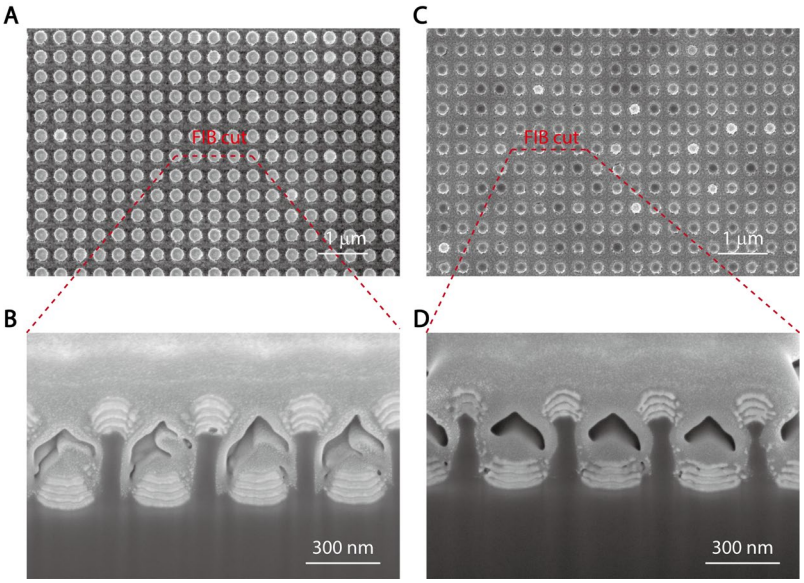

Figure S1. (A) Top-view and (B) cross-sectional view SEM images of nanolaminate plasmonic nanocavities on vertical nanopillars before BOE etching. (C) Top-view and (D) cross-sectional view SEM images of nanolaminate plasmonic nanocavities on vertical nanopillars after 15 s BOE etching of SiO_2 layers. The cutting planes of Figures S1B and S1D are marked by the red dashed lines in Figures S1A and S1C, respectively.

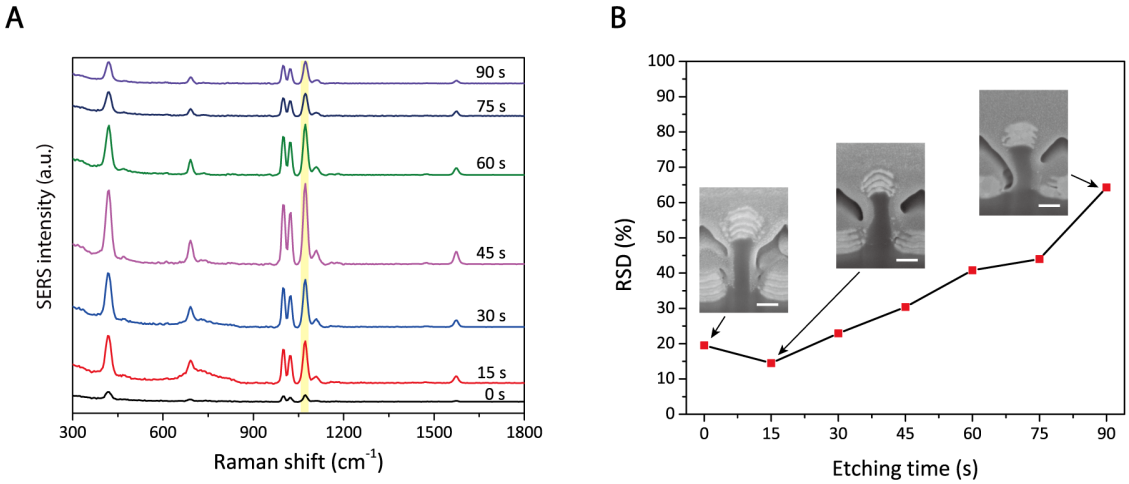

Figure S2. (A) The measured SERS spectra of self-assembled BZT monolayer on Ag/SiO_2/Ag samples under different etching times. (B) The relative standard deviation (RSD) of the Raman intensity at 1077 cm^{-1} (indicated by the yellow shadow) was calculated from 1200 spectra versus etching time, where RSD is the ratio of the standard deviation to the mean. The insets are the cross-sectional view SEM images of the nanolaminate samples with 0 s, 15 s, and 90 s etching (scale bar, 100 nm). The SERS signal intensity keeps increasing as the etching time increases from 0 s to 45 s due to the newly exposed hotspots in the SiO_2 nanogaps by etching, and then decreases as the etching time increases from 45 s to 90 s because of the over-etching induced nanogap collapse which is suggested by the SEM image.

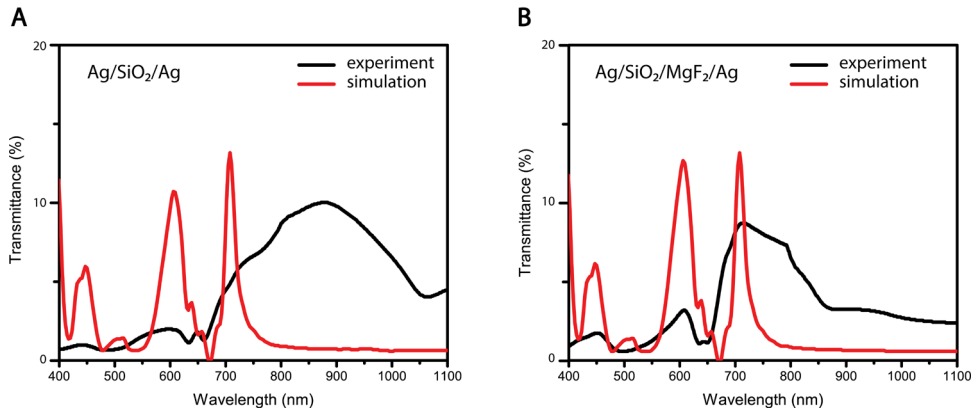

Figure S3. Measured and FDTD-calculated transmission spectra of the (A) $Ag/SiO_2/Ag$ and (B) $Ag/SiO_2/MgF_2/Ag$ nanolaminate plasmonic nanocavities on vertical nanopillars.

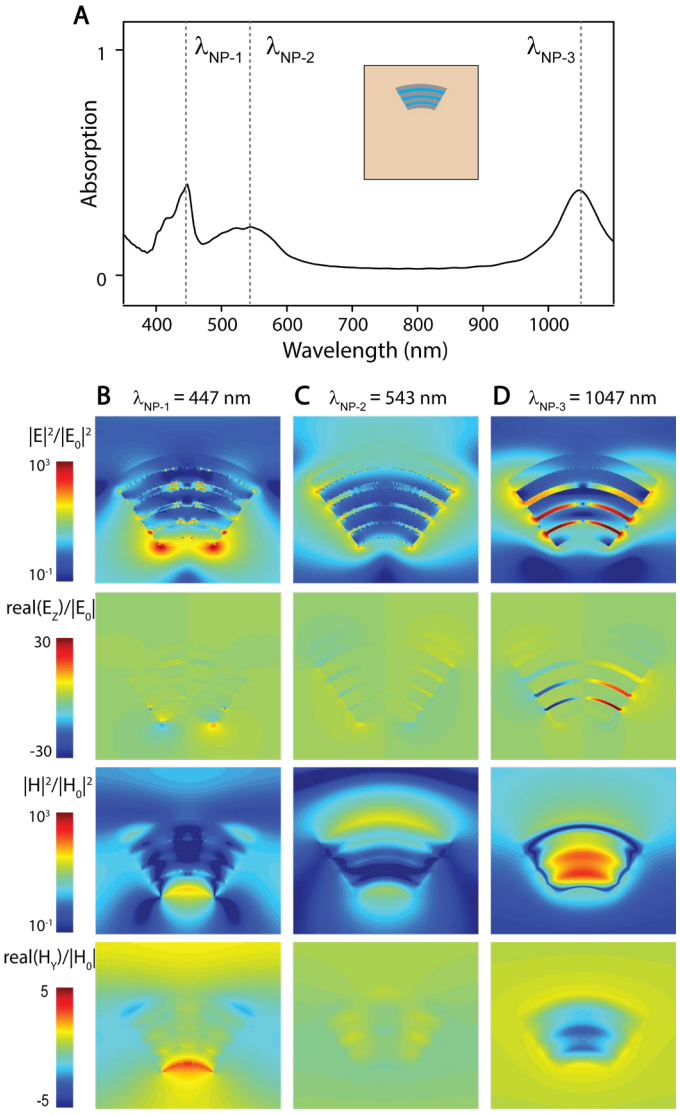

Figure S4. (A) FDTD-calculated absorption spectra of Ag/SiO_2/Ag nanolaminate nanoparticle array. (B-D) The FDTD-calculated x-z distribution maps of $|E|^2$, E_z, $|H|^2$, and H_y for plasmonic modes λ_{NP-1}, λ_{NP-2}, and λ_{NP-3} marked in (A).

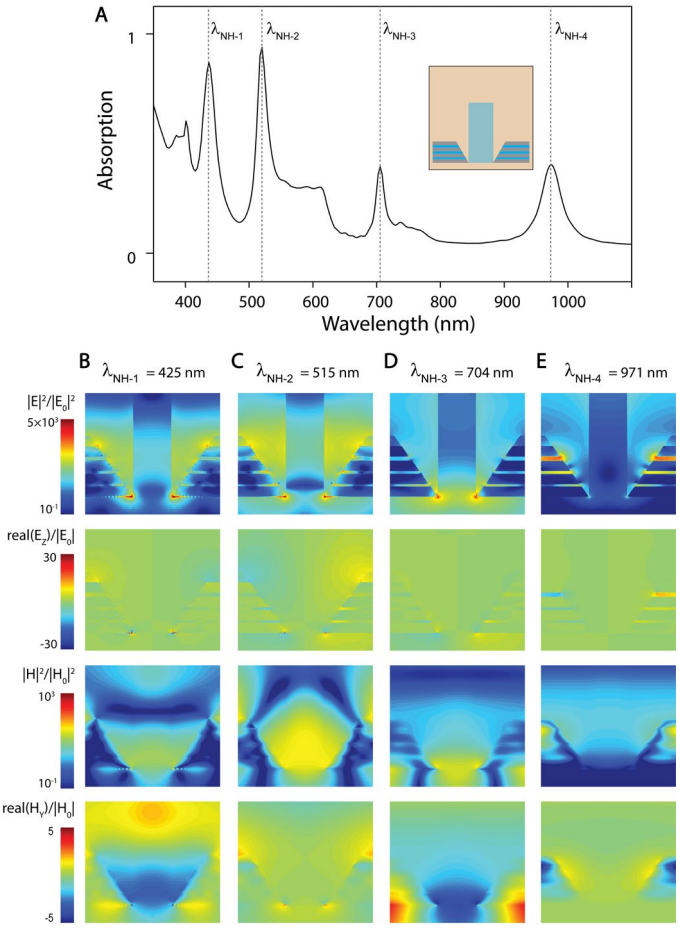

Figure S5. (A) FDTD-calculated absorption spectra of Ag/SiO_2/Ag nanolaminate nanowell array. (B-E) The FDTD-calculated x-z distribution maps of $|E|^2$, E_z, $|H|^2$, and H_y for plasmonic modes λ_{NH-1}, λ_{NH-2}, λ_{NH-3}, and λ_{NH-4} marked in (A).

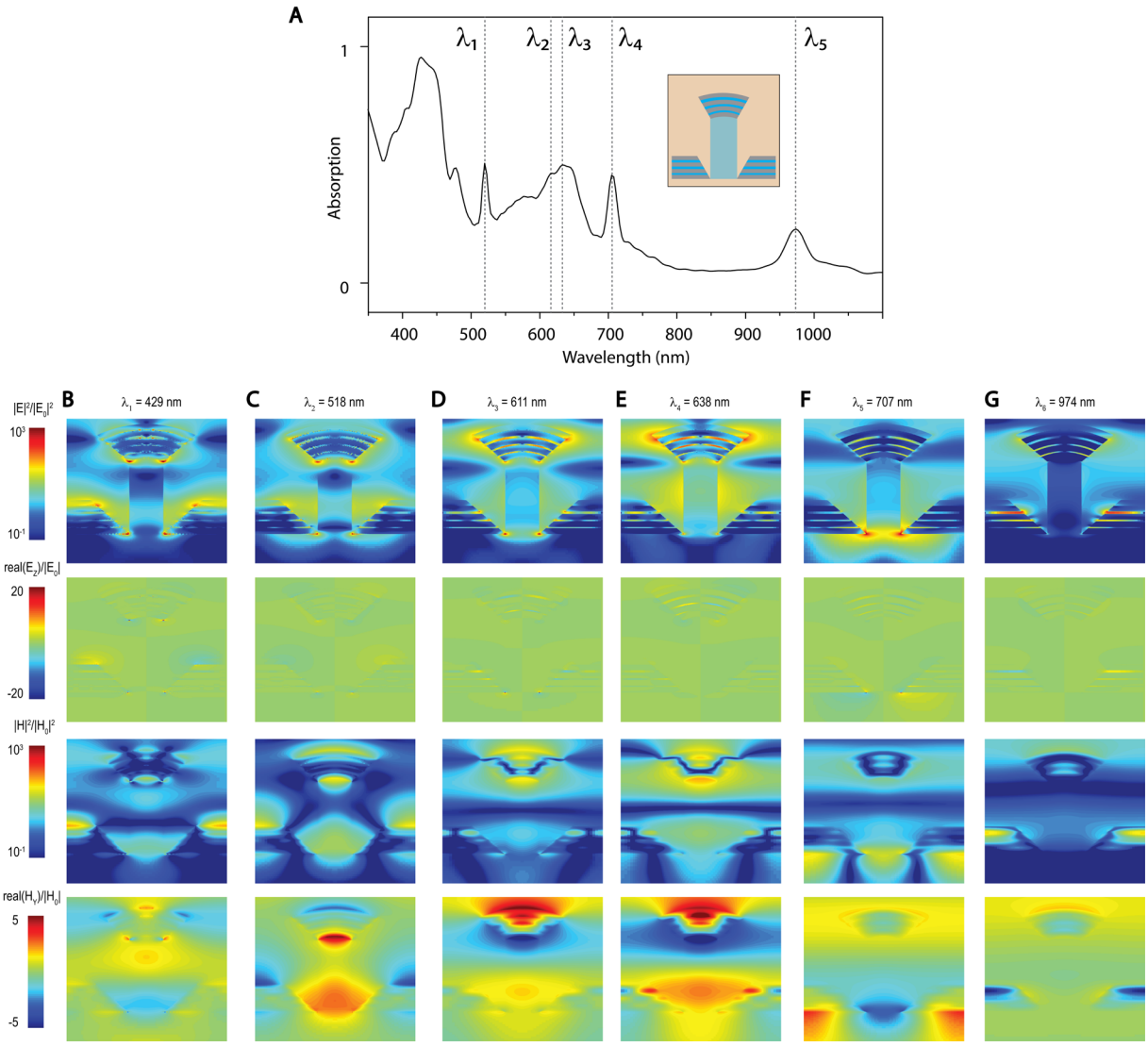

Figure S6. (A) FDTD-calculated absorption spectra of Ag/SiO_2/Ag nanolaminate plasmonic nanocavities on vertical nanopillars. (B-G) The FDTD-calculated x-z distribution maps of $|E|^2$, E_z, $|H|^2$, and H_y for plasmonic modes λ_1 to λ_6 marked in (A).

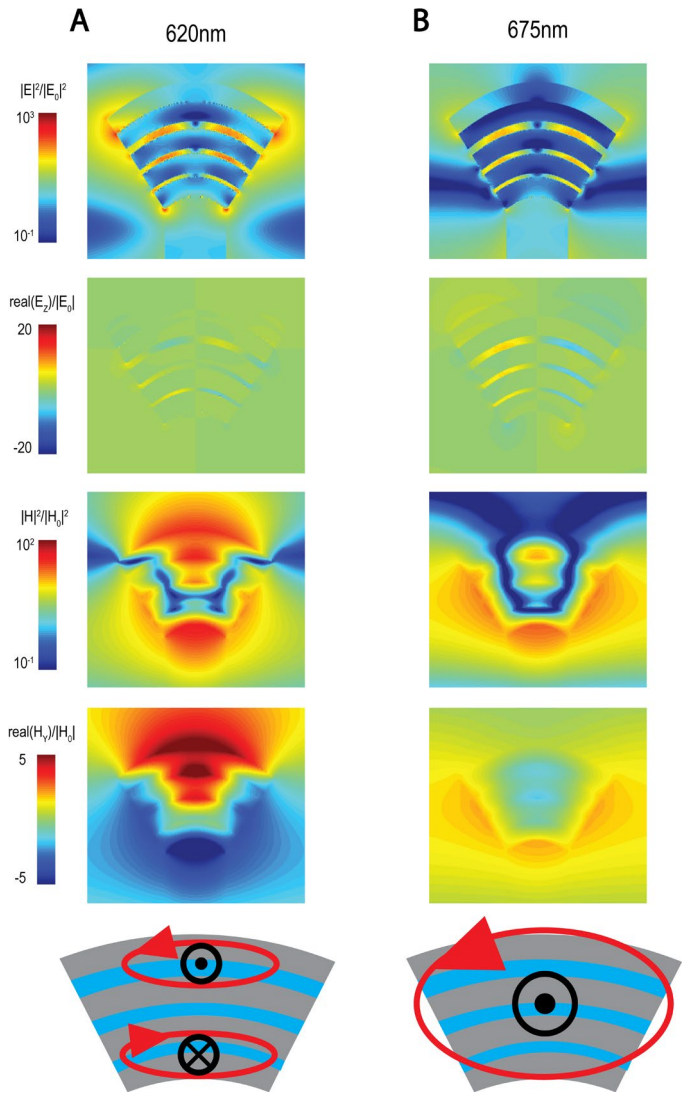

Figure S7. (A) Magnetic Quadrupole (MQ) modes at 620 nm and (B) Magnetic Dipole (MD) mode at 675 nm in the nanoparticle. At 620 nm, the bottom gap and top gap form two out-of-phase MD modes, which we call magnetic quadrupole (MQ) mode in general. The intensity difference comes from the asymmetrical geometry of the nanogap and forms the nodes of fields inside the nanogaps. At 675 nm, all three gaps form three in-phase MD modes, which we call it MD mode in general. The bottom is the schematic figures for the two modes.